A programmable droplet-based microfluidic device applied to multiparameter analysis of single microbes and microbial communities

Kaston Leung[a,b], Hans Zahn[b,c], Timothy Leaver[b,d], Kishori M. Konwar[e], Niels W. Hanson[f], Antoine P. Pagé[e], Chien-Chi Lo[g,h], Patrick S. Chain[g,h], Steven J. Hallam[e,f], and Carl L. Hansen[b,d,1]

[a]Departments of Electrical and Computer Engineering, [b]Centre for High Throughput Biology, [c]Genome Science and Technology Graduate Program, [d]Physics and Astronomy, [e]Microbiology and Immunology, and [f]Graduate Program in Bioinformatics, University of British Columbia, Vancouver, BC, Canada, V6T 1Z4; [g]Genome Science Group, Los Alamos National Laboratory, Los Alamos, NM 87545; and [h]Microbial and Metagenome Program, Joint Genome Institute, Walnut Creek, CA 94598

Edited by David A. Weitz, Harvard University, Cambridge, MA, and approved February 24, 2012 (received for review April 29, 2011)

We present a programmable droplet-based microfluidic device that combines the reconfigurable flow-routing capabilities of integrated microvalve technology with the sample compartmentalization and dispersion-free transport that is inherent to droplets. The device allows for the execution of user-defined multistep reaction protocols in 95 individually addressable nanoliter-volume storage chambers by consecutively merging programmable sequences of picoliter-volume droplets containing reagents or cells. This functionality is enabled by "flow-controlled wetting," a droplet docking and merging mechanism that exploits the physics of droplet flow through a channel to control the precise location of droplet wetting. The device also allows for automated cross-contamination-free recovery of reaction products from individual chambers into standard microfuge tubes for downstream analysis. The combined features of programmability, addressability, and selective recovery provide a general hardware platform that can be reprogrammed for multiple applications. We demonstrate this versatility by implementing multiple single-cell experiment types with this device: bacterial cell sorting and cultivation, taxonomic gene identification, and high-throughput single-cell whole genome amplification and sequencing using common laboratory strains. Finally, we apply the device to genome analysis of single cells and microbial consortia from diverse environmental samples including a marine enrichment culture, deep-sea sediments, and the human oral cavity. The resulting datasets capture genotypic properties of individual cells and illuminate known and potentially unique partnerships between microbial community members.

two-phase flow | droplet wetting | single-cell analysis | qPCR | environmental genomics

Microfluidic devices provide numerous advantages for biological analysis including automation, enhanced sensitivity and reaction efficiency in small volumes (1, 2), favorable mass transport properties (3, 4), and the potential for scalable and cost-effective small volume assays (5). Indeed, advances in microfluidics over the past decade have resulted in increasingly sophisticated functionality and the emergence of two dominant and orthogonal strategies for fluid handling, based either on the use of integrated microvalves or the transport of microdroplets, both in closed channels or over electrode surfaces.

The development of soft lithography (6) and the extension of this method to the fabrication of integrated microvalves using multilayer soft lithography (5) has enabled devices with thousands of active microvalves per cm^2. This high level of integration enables device architectures capable of executing thousands of predefined "unit cell" reactions in parallel, with applications ranging from protein structure (4) and interaction studies (7, 8) to single-cell analysis and genomics (2, 9, 10). Two-phase flow systems that manipulate picoliter (pL) volume droplets in closed channels have been shown to be ideally suited to high-speed serial analysis for use in high-throughput screening applications (11) and sample preparation for genomics (12), while the programmable manipulation of nanoliter (nL) volume droplets using electrostatic forces has received increasing attention as a potential platform for sample processing automation in proteomics and medical diagnostics (13).

Despite the transformative potential of microfluidic devices, application innovation and user adoption have lagged due to limited access to these technologies. With the exception of a handful of commercially available products (12, 14), the use of microfluidic devices has remained tethered to beta testers and engineering laboratories. This is largely due to the prevailing paradigm in microfluidic research in which devices are "hardwired" for specific fluid handling tasks, necessitating a customized design for each application or change in protocol. This application-specific approach requires iterative cycles of device design, fabrication, and testing, presenting a major obstacle to the development of new applications and limiting user adoption and community access. In analogy to how programmable integrated circuits enabled a broader community of developers and nonexpert users, the advancement of programmable microfluidic devices stands to dramatically enhance the pervasiveness and impact of microfluidic systems (15).

Here, we report the development of a scalable and programmable multipurpose microfluidic device capable of running multiple user-defined single-cell applications: phenotypic sorting of bacteria followed by clonal analysis of growth rates, taxonomic identification of single bacteria by small subunit ribosomal RNA gene quantitative PCR (qPCR) and sequencing, and high-throughput single-cell whole genome amplification (WGA) and sequencing. We apply this system to the genomic analysis of single cells and microbial consortia from environmental samples and demonstrate how scalable microfluidic single-cell manipulation and processing may be used to illuminate relationships between microbial community members.

Results and Discussion

Device Architecture and Operation. ***Device design.*** The functionality of our device is achieved by combining the advantages of droplet-based sample compartmentalization with the reconfigurable flow-routing control enabled by integrated microvalves. The device allows metering of programmable volumes of eight reagents,

Author contributions: K.L., A.P., S.H., and C.L.H. designed research; K.L., H.Z., and T.L. performed research; K.L., K.M.K., N.W.H., A.P., C.-C.L., P.S.C., S.H., and C.L.H. analyzed data; and K.L., A.P., S.H., and C.L.H. wrote the paper.

The authors declare no conflict of interest.

This article is a PNAS Direct Submission.

[1]To whom correspondence should be addressed. E-mail: chansen@phas.ubc.ca.

This article contains supporting information online at www.pnas.org/lookup/suppl/doi:10.1073/pnas.1106752109/-/DCSupplemental.

assembly and storage of these reagents in any one of 95 addressable storage chambers, and off-chip recovery of reaction products from selected individual chambers. The device features a 2D addressable array of chambers, a reagent-metering module, a cell-sorting module, and an integrated nozzle that allows for automated recovery of on-chip reaction products without cross-contamination (Fig. 1). Prior to use, the entire chip is primed with a water-immiscible oil phase that serves as the carrier fluid for reagent droplets. Programmable reagent dispensing, using a three-valve peristaltic pump, is used to deliver arbitrary volumes of reagents in discrete increments from eight separate reagent inlets by varying the number of pump cycles; each "pump increment" advances approximately 133 pL of fluid (16) (Fig. 1*F*). Reagent droplets are dispensed directly into a flowing stream of carrier fluid, where they break off through the combined effect of surface tension, shear flow, and valve actuation (Movie S1).

Droplets are delivered to a selected storage chamber by use of a fluidic multiplexer (16, 17) to select the desired row and a series of column valves to select the desired column. This creates a unique fluidic path that passes from the high-pressure oil input, past the droplet metering module, to the selected chamber, and out to one of two low-pressure outlets (waste or elution) (Fig. 1*B*). Each reagent droplet is transported along this path and is deposited in the chamber where it merges with any previously dispensed droplets. At any time, the contents of any addressed chamber can be recovered from the chip through an integrated elution nozzle, designed to dispense directly into standard microfuge tube formats (Fig. 1*A*).

For single-cell applications, the phenotypic selection and isolation of single cells is achieved using a cell-sorting module (Fig. 1*E*). A cell suspension is advanced by peristaltic pumping and imaged in real time at the channel cross-junction. When a cell of interest is identified, it is pumped into a droplet for delivery to the storage chamber array.

Droplet docking and merging by flow-controlled wetting. Programmability of the microfluidic device is enabled by the ability to precisely position and merge an arbitrary sequence of droplets at each addressable storage location. We achieve this by exploiting the properties of two-phase hydrodynamic flow to implement a simple and robust method that prevents droplet wetting during transport, which can result in reagent cross-contamination (3), while preserving the ability to wet channel walls at precisely defined storage locations. A droplet flowing down a channel filled with an immiscible carrier fluid is separated from the channel walls by a thin lubricating film, the thickness of which is a function of droplet velocity (18). If the droplet velocity, and hence the film thickness, is reduced below a critical value, an instability arises in which intermolecular forces between the droplet and the surface cause the film to spontaneously rupture, allowing the droplet to wet the channel walls (19) (*SI Text*). Selective wetting may therefore be achieved without modification of surface properties by engineering the device geometry such that droplet velocity remains above this critical value until arrival at the storage area.

Storage elements were designed to decelerate incoming droplets by diverting oil flow through bypass channels (20). Each storage element consists of a large cross-section cylindrical storage chamber that is connected to an inlet channel featuring a series of small side channels, which connect the inlet channel to a pair of bypass channels that flow around each side of the storage chamber (Fig. 1*C*). As the droplets move into the inlet channel, carrier fluid is diverted through the side channels, causing the droplet to slow (Fig. 1*C*, *step 2*). Droplets do not pass through the side channels due to the high interfacial tension required for deformation.

When droplets enter the storage element with a velocity less than or equal to a critical value, they wet the inlet channel upstream of the storage chamber. As the leading edge of a droplet enters the chamber, it is pulled in by surface tension (Movies S2 and S3), where it wets the chamber's sidewall, precisely positioning it at the chamber entrance (Fig. 1*C*, *step 3i*). Once docked inside the chamber, the droplets are sequestered from high-shear flows (Fig. S1) and are immobilized indefinitely. Contact line pinning forces are sufficient to resist shear forces at a mean flow velocity of 50 mm/s measured at the storage element inlet. It should be noted that surface tension forces between the droplet and the carrier phase do not contribute to retention of the droplet at the chamber entrance as advancement of the droplet further into the chamber would not increase the droplet's interfacial area

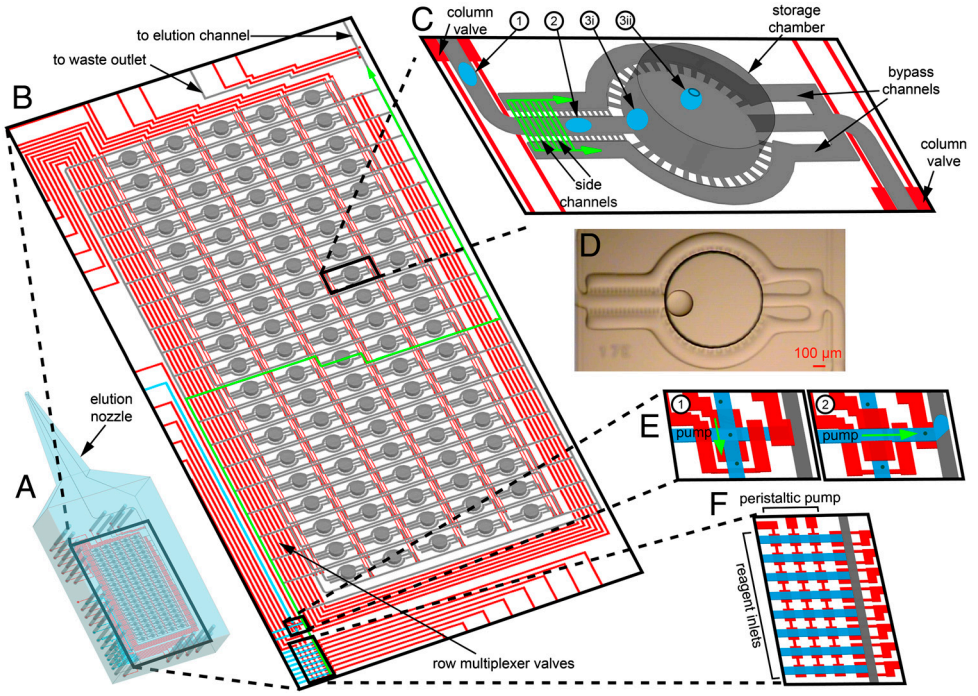

Fig. 1. Programmable microfluidic reaction array. (*A*) Device schematic showing the structure of an elution nozzle designed to interface with standard microfuge tubes during chamber elution. (*B*) Addressable array of 95 storage chambers organized in 19 rows and 5 columns. Control layers are shown in red. Actuation of row multiplexer and column valves creates a unique fluidic path (green arrow) flowing from high to low-pressure ports. (*C*) Storage element geometry for droplet immobilization and coalescence by flow-controlled wetting. (1) During transport to an addressed storage element, a lubricating thin film of oil prevents wetting of channel walls. (2) Side channels create a bypass for the oil (green arrows), reducing droplet velocity. (3i) Below the critical flow velocity, wetting occurs and the droplet is positioned at the cylindrical chamber entrance. (3ii) Above the critical flow velocity, the droplet does not wet at the entrance but travels into the chamber and docks at the chamber ceiling. (*D*) Micrograph of a 2.7-nL stored water droplet. (*E*) Cell-sorting module. (1) A single-cell suspension is pumped down the sorting channel. (2) The cell is encapsulated in a droplet for transport to the chamber array. (*F*) Reagent-metering module.

(*SI Text*). Each subsequent droplet is delivered to the same position and held in contact with the stored droplet, thereby ensuring sufficient time for coalescence even when partially stabilizing surfactants are used.

The volume of the storage chamber defines an upper limit on the volume of the stored droplet, above which further droplet additions result in the ejection of droplets into the carrier fluid as it exits the chamber. In the present design, this upper limit is approximately 40 nL, corresponding to 300 pump increments and a formulation resolution of 1 in 300.

If droplets enter the storage element with a velocity above the critical value, they are not sufficiently decelerated by the side channels and enter the chamber without wetting the channel walls. In this case, the free droplets follow an upward trajectory determined by a combination of laminar flow and buoyancy, coming to rest at the chamber ceiling where they wet and are immobilized (Fig. 1*C*, *step 3ii* and Movie S4). In this regime, the robust merging of all droplets is guaranteed only once the stored volume occupies a significant fraction of the storage chamber (approximately 25%). Thus, if the final stored droplet volume is sufficiently large and the sequence of droplet merging is unimportant, storage chambers can be filled at the maximum flow rate supported by the device (Movie S5).

Selective recovery of reaction products. Elution of any stored droplet is achieved by flushing an addressed storage chamber with a continuous oil-sheathed stream of buffer. This stream, formed by applying equal pressures to a buffer and an oil inlet that join at a T-junction (21), coalesces with the stored droplet until it exceeds the chamber capacity. At this point, an oil-sheathed aqueous stream, containing the stored droplet's contents, is ejected from the storage chamber and directed to the elution channel (Movie S6 and Fig. S2*A*). The oil surrounding this eluted stream preferentially wets the downstream channel walls, preventing sample cross-contamination through surface adsorption. Elution of the 40 nL chamber contents by flushing with approximately 500 nL of buffer results in better than 99.8% sample recovery as determined by fluorescent measurements with fluorescein-labeled 40-mer oligonucleotides. We note that for any off-chip analysis the resulting dilution is unavoidable due to practical limitations on the minimum volumes that can be handled off-chip (approximately 1 μL). To enable automated recovery directly into microfuge tubes, the device is mounted to a custom 3-axis robotic chip-holder (Fig. S2*B*) controlled by software that coordinates stage motion with valve actuation. A zero dead-volume elution nozzle, built into the chip and designed to fit into standard microfuge tube formats (Fig. 1*A*), allows deposition of reaction products from each chamber into a separate tube.

Device Performance. To establish the metering precision of the device, we formulated a series of 26.6 nL stored droplets, having 10 different fluorescent dye concentrations ranging from 100 nM to 1 μM, each formed by dispensing programmed numbers of pump increments of 1 μM dye or diluting buffer. The resulting dye concentrations, as measured by mean fluorescent intensity, were found to be in excellent agreement with target values over the full range ($R^2 = 0.999$) (Fig. 2*A*), with an average coefficient of variation of 1.4%. As a demonstration of arbitrary and addressable formulation, we applied the device as a programmable display (Fig. 2*B*).

We next used on-chip qPCR as a sensitive assay to establish the upper bound of cross-contamination during reaction formulation and product recovery. Fifty chambers were alternately loaded in a checkerboard pattern, each receiving PCR reagents premixed with either genomic DNA (approximately 1,476 genome equivalents) or no template. End-point fluorescent imaging after PCR showed that all template-containing chambers were successfully amplified while none of the no-template control (NTC) chambers

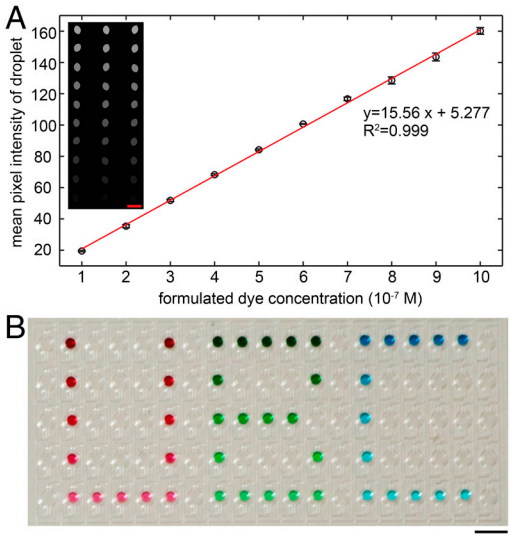

Fig. 2. Addressable and precise formulation. (*A*) Metering precision. Mean fluorescent intensity and standard deviation of fluorescent measurements of 26.6-nL droplets, composed of 200 pump increments of 1-μM dye or diluting buffer ($N = 3$). (*Inset*) Corresponding fluorescent confocal image of the array of stored droplets. Scale bar, 1 mm. (*B*) Microfluidic display showing addressable and programmable formulation. Stored droplets are composed of 300 pump increments arranged in letters with a twofold dilution series of dye from top to bottom of each letter. Scale bar, 2 mm.

amplified (Fig. S3*A*). Based on demonstrated efficient PCR with single molecule sensitivity (Fig. S4), we determined the upper bound on cross-contamination to be 1 in 1,476.

Next, we measured cross-contamination between chambers during elution. First, 47 chambers were loaded with 13.3 nL of water and another 47 were then loaded with an equal volume of qPCR solution containing DNA template (18 genome equivalents) in a checkerboard pattern of alternating water and PCR droplets. Following 40 cycles of on-chip PCR amplification, pairs of PCR product and water droplets were alternately eluted from the device into separate microfuge tubes. qPCR was then used to assess the degree of carry-over between tubes. The absolute mean fold concentration difference for all eluted pairs, calculated as $2^{\Delta CT}$, was 4.84×10^5 with a standard deviation of 19.8 (Fig. S3*B*).

Application to Multiparameter Single Microbe Analysis. ***Sorting and culture of single bacteria.*** Droplets are particularly well suited to the isolation and manipulation of bacteria (22), which, due to their small size, are difficult to manipulate by alternative hydrodynamic trapping mechanisms on-chip. To demonstrate morphological or fluorescence-based sorting and isolation of single cells from a mixed population, we first performed a series of cell culture experiments in which defined numbers of single *Salmonella typhimurium* cells, selected from a mixture of two strains expressing either green or red fluorescent protein (GFP or RFP), were isolated and grown in microdroplet reactors. The strains are genetically identical with the exception of the encoded fluorescent protein. A total of 85 cell cultures were seeded, consisting of different starting cell types and numbers: monoclonal cultures seeded with single GFP- or RFP-expressing cells ($N = 20$ for each) (Fig. 3*C*), single strain cultures of approximately 100 GFP- or RFP-expressing cells ($N = 5$ for each), and mixed cultures having one cell of each strain ($N = 20$), and approximately 10 ($N = 5$), 100 ($N = 5$), and 1,000 ($N = 5$) cells of each strain. Each starting cell population was loaded into a separate storage chamber and filled with growth media to a final volume of 40 nL. The device was then incubated at 25 °C and imaged every 10 min for 23.3 h to generate growth curves based on the total GFP and RFP expression in each culture (Fig. 3 *A* and *B*). An end-point

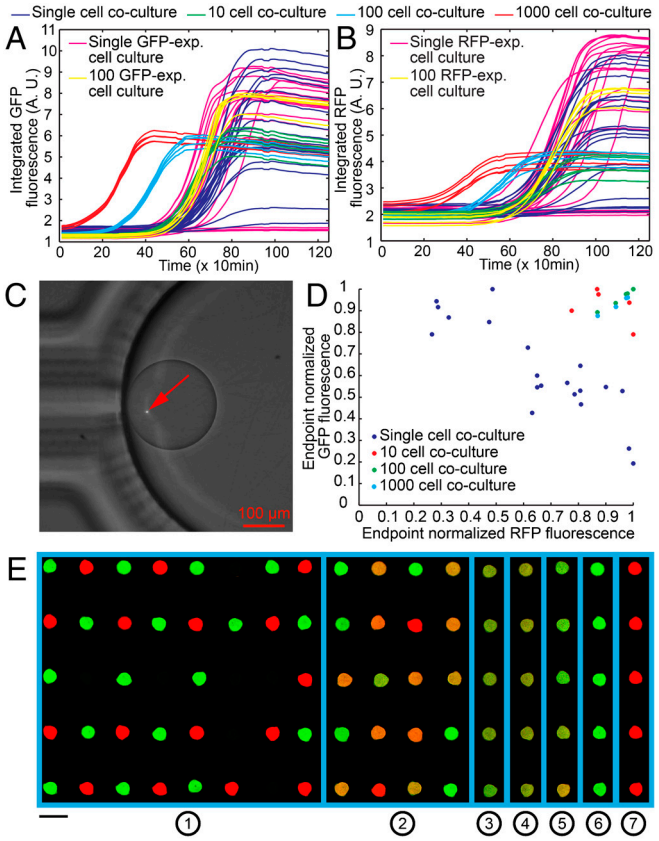

Fig. 3. On-chip culture of single sorted bacteria. Growth curves of each on-chip culture seeded with GFP-expressing (*A*) and RFP-expressing (*B*) cells. (*C*) Combined brightfield and fluorescent micrograph of a single RFP-expressing cell in a stored droplet. (*D*) Scatter plot of normalized end-point fluorescence intensity in GFP and RFP channels for mixed cultures seeded with different numbers of both strains. (*E*) Overlaid GFP and RFP-channel confocal images of all cultures in the stored droplet array after incubation. Cultures were seeded with (1) single cells (dark parts of the array are unsuccessful cultures), (2) a single cell of each strain, (3) approximately 1,000 cells of each strain, (4) approximately 100 cells of each strain, (5) approximately 10 cells of each strain, (6) approximately 100 GFP-expressing cells, and (7) approximately 100 RFP-expressing cells. Scale bar, 1 mm.

confocal image of the droplet array shows that no GFP fluorescence was detected in the RFP-expressing monoclonal cultures and vice versa, indicating contamination-free cell sorting (Fig. 3*E*).

Comparable plating efficiency was observed for both the GFP- and RFP-expressing strains, with colony formation observed in 17 of 20 (85%) and 16 of 20 (80%) of the single-cell GFP and RFP cultures (respectively). Successful monoclonal cultures exhibited heterogeneous growth curves, showing that differences in the proliferative capacity of single microbes can be significant even in isogenetic populations. These differences resulted in stochastic variability in the final composition of mixed cultures loaded with equal but varying numbers of cells (1, 10, 100, 1,000) from each strain (Fig. 3*D*); variability was largest when starting from single-cell cultures and was progressively reduced as the size of the starting populations increased. This simple experiment illustrates how stochastic differences between individual cells can lead to large differences in the success of two organisms populating a new microenvironment, even in the case of equal fitness.

PCR-based genotyping of single bacteria. As a second demonstration of single-cell analysis we performed genotyping experiments based on PCR amplification and sequencing of small subunit ribosomal RNA (SSU rRNA or 16S) genes from bacteria sorted from a mixed population of *Escherichia coli* and RFP-expressing *S. typhimurium*. Thirty single *S. typhimurium* and 29 single *E. coli* were sorted into chambers and mixed with PCR reagents containing an intercalating dye and primers targeting a 144-bp segment of the 16S gene. The target sequence was amplified in 16 of 30 (53%) single *S. typhimurium*, and 25 of 29 (86%) single *E. coli*, as determined by qPCR curves for each reaction. Following PCR, the amplicons from each reaction were eluted and six successful single-cell reactions from each species were chosen at random for further off-chip amplification and capillary sequencing. All six single *E. coli* cells and five of six single *S. typhimurium* cells were correctly identified; the single *S. typhimurium* amplicon that could not be identified also did not match the expected sequence for *E. coli*.

Overall, the success rate of PCR amplification from single cells was 41 of 59 (69%), which is comparable to previous reports (14, 22). To determine whether reaction failures were due to inefficient heat lysis, inaccessibility of genomic DNA, or suboptimal PCR performance, we ran additional experiments in which a strain-specific fragment of the *E. coli* 16S gene was amplified in single *E. coli* cells using an optimized primer set (23). A total of 77 reactions were formulated using either single cells ($N = 62$), approximately 100 cells ($N = 5$), or cell suspension fluid containing no cells ($N = 10$). qPCR curves showed that the target sequence was successfully amplified in 60 of 62 (97%) single cells, 4 of 5 (80%) multiple cell reactions, and none of the no-cell control reactions (Fig. S5). The ΔCT between the single and 100-cell reactions (Fig. S5, *Inset*) was found to be 6.52 ± 2.06, indicating an assay efficiency of 102.7%. Capillary sequencing of 10 randomly selected single-cell reactions was performed following an additional round of off-chip amplification and all samples were confirmed to have the expected sequence.

Single-cell whole genome amplification. As a final demonstration of single-cell analysis we applied our device to single-cell WGA followed by product recovery and shotgun sequencing. We first evaluated the performance of our platform using a commercially available PCR-based WGA protocol that has not previously been applied in microfluidic applications (Picoplex, Rubicon Genomics). Using two devices we performed WGA on 127 single *E. coli* cells, no-cell control reactions containing only cell suspension fluid, and reactions loaded with approximately 1,000 cells. qPCR on eluted WGA product indicated that 73 of 127 (57%) single-cell reactions and none of the 21 no-cell control reactions resulted in at least a 100-fold amplification of the 16S gene. We note that this should be regarded as a lower bound because PCR-based WGA amplification is known to exhibit large bias (24) and may result in preferential amplification of genomic regions other than the one targeted by our assay.

Product from six successful single-cell reactions, two no-cell control reactions, and one 1,000-cell reaction were chosen for sequencing, along with a bulk sample of unamplified *E. coli* gDNA, using an Illumina Genome Analyzer 2 instrument. Sequencing libraries for each single cell were constructed both from reaction product eluted directly from the chip and from samples that had been subjected to a second round of WGA off-chip. Sequencing statistics for each of these samples is summarized in Table S1, with genome coverage ranging from 15.2% to 64.6% for the on-chip WGA product and from 24.5% to 62.8% after a second round of WGA. No-cell controls showed no significant alignment to the reference genome. We note that the single-cell reactions with the highest coverage were comparable to the 1,000-cell reaction, indicating that coverage is likely limited by amplification bias and sequencing depth.

Environmental applications. Following initial optimization and biological testing of the microfluidic device we conducted WGA and sequencing using environmental samples to explore genomic relationships within natural microbial communities.

Samples were selected from three environments representing varying levels of structural complexity and sorted on-chip. Environment 1 (ENV1) was a bacterial enrichment culture from seawater chosen to represent a low-complexity environment. Environment 2 (ENV2) was a 3–8 μm fraction from deep-sea sediments associated with methane seepage. Environment 3 (ENV3) was a human oral biofilm chosen to represent a high-complexity microenvironment. Details of sample preparation for each environment are provided in *SI Text*.

Based on the complexity and aggregation state of each environment we used alternative sorting approaches. Single cells were isolated from ENV1, individual spherical aggregates were isolated from ENV2, and individual extended filamentous aggregates were isolated from ENV3. A total of 203 on-chip WGA reactions were performed (50 in ENV1, 93 in ENV2, and 60 in ENV3) including five NTCs consisting of equal volumes of cell suspension fluid containing no visible cells.

A total of 74 samples representing each of the environments were randomly selected for a subsequent round of off-chip amplification and sequencing library construction, resulting in 72 successful libraries: 24 single cells from ENV1, 23 spherical aggregates from ENV2, 22 filamentous aggregates from ENV3, and 3 no-cell control samples. The two remaining samples were excluded due to suspected contamination or mislabeling during library preparation. Samples were indexed, pooled, and sequenced on a single lane of an Illumina Genome Analyzer II instrument, generating a total of 4.8 billion bases in 64 million reads (Table S2).

We first analyzed the genomic complexity of indexed samples by plotting kernal density functions of GC composition. All ENV1 samples exhibited a single characteristic peak, consistent with targeted amplification of closely related donor genotypes (Fig. 4*A* and Fig. S6). By comparison, the GC content exhibited by ENV2 samples was a mixture of unimodal and multimodal curves consistent with amplification of multicellular aggregates (Fig. 4*A* and Fig. S7). Finally, ENV3 samples also exhibited multimodal curves and single-spreading peaks consistent with targeted amplification of both single-cell genomes and mixtures of adhering cells (Fig. 4*A* and Fig. S8). The taxonomic structure of each sample was then determined using a tripartite binning approach. We initially adopted a stringent binning criteria based on 40 conserved phylogenomic markers mapped onto the tree of life using MLTreeMap (25). However, due to low sequencing depth only a handful of these markers were identified. To increase taxonomic resolution we queried the eggNOG (26) and NCBI ref_seq databases using open reading frames predicted on contigs from each indexed sample. Results from the ref_seq search were then mapped onto the NCBI taxonomic hierarchy using metagenome analyzer (MEGAN) to define the most probable ancestor for each query sequence (27). Open reading frames (ORFs) assigned to taxonomic nodes by MEGAN were normalized by the fraction within each sample and hierarchically clustered, resulting in three distinct clusters for the ENV1, ENV2, and ENV3 samples. Branch lengths within each of the three clusters were consistent with increasing levels of genomic complexity with ENV1 samples exhibiting the least complexity followed by ENV3 and ENV2 (Fig. 4*B*).

The taxonomic origins of ORFs predicted in ENV1 samples were primarily affiliated with the genus *Pseudoalteromonas* within the Gammaproteobacteria (Fig. 4*C* and Fig. S9 and Table S3). Based on hierarchical clustering results, two genotypic variants were resolved, consistent with the presence of closely related subpopulations within the enrichment culture. ORFs from ENV2 samples were dominated by sulfate reducing bacteria (SRB) affiliated with *Desulfatibacillum*, *Desulfobacterium*, and *Desulfococcus* within the Deltaproteobacteria (Fig. 4*C* and Fig. S10 and Table S3). Intermediate levels of representation were observed for unaffiliated Gammaproteobacteria and Betaproteobacteria in addition to methanogenic archaea. Low-level representation

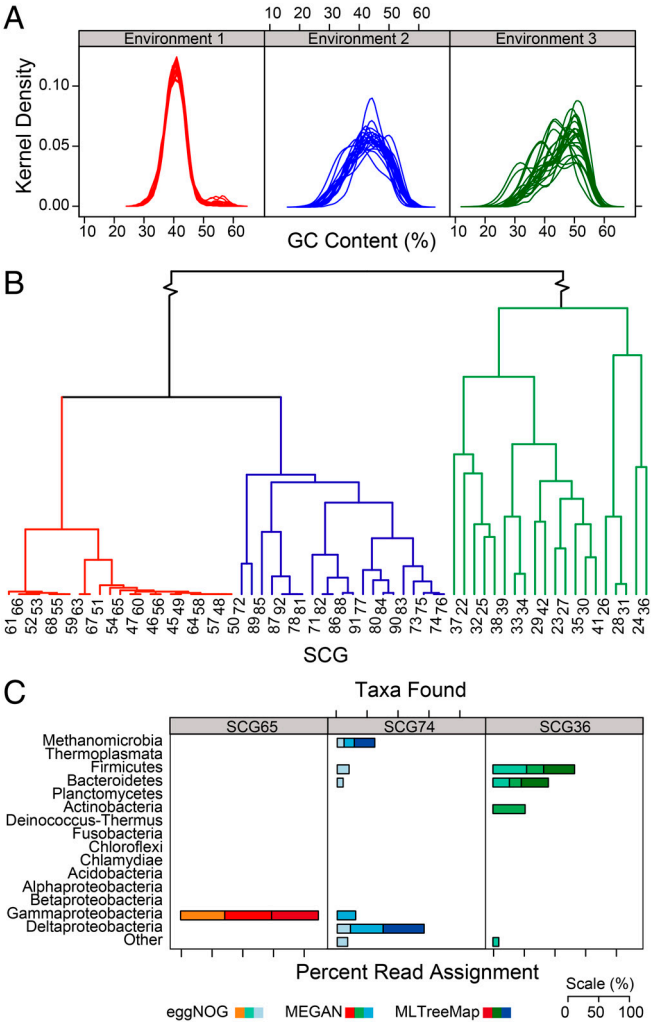

Fig. 4. Summary of taxonomic profiles uncovered in metagenomes of 67 WGA samples originating from three distinct environments. (*A*) Superimposed GC kernel density plot for all contigs generated from assemblies of individual metagenomic datasets. (*B*) Hierarchical cluster analysis of sample-specific taxonomic profiles generated through a MEGAN analysis of blastx sequence comparisons against the RefSeq proteomic database (samples with no signal were excluded). Due to the size of intercluster distance between ENV1, ENV2, and ENV3 branch lengths are not drawn to scale. (*C*) Taxonomic profiles of three environment-representative metagenomes, as generated through three distinct procedures (MLTreeMap, blastx against egg NOG, blastx against RefSeq proteomic).

of other taxa was observed in specific ENV2 samples, including ORFs affiliated with Alphaproteobacteria, Bacteroidetes, Firmicutes, Chloroflexi, and Clostridia. Given the low sequence coverage for each sample and limited database representation of reference genomes for relevant sediment bacteria and archaea, it remains to be determined to what extent these configurations represent known or novel modes of structural integration (28, 29). ORFs from ENV3 samples were dominated by known human oral microbiome constituents including Capnocytophaga and Flavobacterium within the Bacteroidetes, Corynebacterium, Rothia, Kocuria and Actinomyces within the Actinobacteria, Fusobacterium within the Fusobacteria, and Clostridium and Streptococcus within the Firmicutes (Fig. 4*C* and Fig. S11 and Table S3). Low-level representation of the candidate division TM7 was also observed. Different samples contained overlapping, but not identical, subsets of these taxonomic groups, with Streptococcus, Corynebacterium, and Capnocytophaga being the most common overlapping taxa. Many of the taxonomic config-

urations observed in ENV3 samples have been previously described in the context of coaggregation and biofilm formation within the oral cavity (30–33), and several have been directly visualized using combinatorial labeling and spectral imaging techniques (34).

Conclusion

The development of universal and programmable microfluidic devices holds great promise for accelerating the development and adoption of microfluidic applications. Toward this goal, we have presented a versatile microfluidic device that allows for the execution of different experiments, and the independent recovery of reaction products, through simple software reprogramming of device operation. This capability is achieved by the development of a robust and simple droplet immobilization strategy that is based on flow-controlled wetting, which is distinct from previously described techniques based on surface tension (20, 35, 36) or hydrodynamic trapping (37); we note that, depending on the choice of surfactant and carrier phase, surface wetting may also play a role in other reported droplet storage designs, although this has not been previously recognized.

The demonstrated capabilities for sorting, isolation, and programmable processing of single cells in droplets offers a versatile platform for the analysis of single microbes on-chip. The genomic approaches presented here are also equally applicable to eukaryotic cells and nuclei. Furthermore, the ability to place multiple selected single cells in the same nanoliter volume provides opportunities for studying intercellular interactions at the single-cell level. We anticipate that the flexibility of this platform will enable a myriad of other biological applications including enzyme characterization, the optimization of molecular biology protocols, and chemical synthesis. We contend that the availability of programmable microfluidic devices such as the one described here will democratize microfluidics research, providing a common hardware solution on which software and "wetware" may be developed and shared by a larger user community.

Materials and Methods

Details of microfluidic fabrication and operation, calculations, reagent composition, image acquisition and analysis, cell preparation, and sequence analysis are provided in *SI Text*.

ACKNOWLEDGMENTS. We thank Bud Homsy for invaluable discussions regarding droplet wetting, Nat Brown for bacterial strains and assay design, Mike Vaninsberghe for assistance with image analysis, and Jens Huft for assistance with device imaging. This research was funded by the Natural Sciences and Engineering Research Council (NSERC), Genome BC, Genome Alberta, Genome Canada, Western Diversification, the Canadian Institute for Health Research (CIHR) and the Canadian Institute for Advanced Research. Salary support was provided by the Michael Smith Foundation for Health Research (C.H.), Canada Research Chairs (S.H.), NSERC (K.L.), CIHR (C.L.H.), Genome Canada (A.P. and N.H.) and the Tula foundation funded Centre for Microbial Diversity and Evolution (K.K.)

1. Marcy Y, et al. (2007) Nanoliter reactors improve multiple displacement amplification of genomes from single cells. *PLoS Genet* 3:1702–1708.
2. White AK, et al. (2011) High-throughput microfluidic single-cell RT-qPCR. *Proc Natl Acad Sci USA* 108:13999–14004.
3. Tice JD, Song H, Lyon AD, Ismagilov RF (2003) Formation of droplets and mixing in multiphase microfluidics at low values of the Reynolds and the capillary numbers. *Langmuir* 19:9127–9133.
4. Hansen CL, Skordalakes E, Berger JM, Quake SR (2002) A robust and scalable microfluidic metering method that allows protein crystal growth by free interface diffusion. *Proc Natl Acad Sci USA* 99:16531–16536.
5. Thorsen T, Maerkl SJ, Quake SR (2002) Microfluidic large-scale integration. *Science* 298:580–584.
6. Xia YN, Whitesides GM (1998) Soft lithography. *Annu Rev Mater Sci* 28:153–184.
7. Maerkl SJ, Quake SR (2007) A systems approach to measuring the binding energy landscapes of transcription factors. *Science* 315:233–237.
8. Singhai A, Haynes CA, Hansen CL (2010) Microfluidic measurement of antibody-antigen binding kinetics from low-abundance samples and single cells. *Anal Chem* 82:8671–8679.
9. Marcy Y, et al. (2007) Dissecting biological "dark matter" with single-cell genetic analysis of rare and uncultivated TM7 microbes from the human mouth. *Proc Natl Acad Sci USA* 104:11889–11894.
10. Fan HC, Wang J, Potanina A, Quake SR (2011) Whole-genome molecular haplotyping of single cells. *Nat Biotechnol* 29:51–57.
11. Agresti JJ, et al. (2010) Ultrahigh-throughput screening in drop-based microfluidics for directed evolution. *Proc Natl Acad Sci USA* 107:4004–4009.
12. Tewhey R, et al. (2009) Microdroplet-based PCR enrichment for large-scale targeted sequencing. *Nat Biotechnol* 27:1025–1031.
13. Shih SCC, et al. (2012) Dried blood spot analysis by digital microfluidics coupled to nanoelectrospray ionization mass spectrometry. *Anal Chem* 84:3731–3738.
14. Ottesen EA, Hong JW, Quake SR, Leadbetter JR (2006) Microfluidic digital PCR enables multigene analysis of individual environmental bacteria. *Science* 314:1464–1467.
15. Fidalgo LM, Maerkl SJ (2011) A software-programmable microfluidic device for automated biology. *Lab Chip* 11:1612–1619.
16. Lau BTC, Baitz CA, Dong XP, Hansen CL (2007) A complete microfluidic screening platform for rational protein crystallization. *J Am Chem Soc* 129:454–455.
17. Hua Z, et al. (2006) A versatile microreactor platform featuring a chemical-resistant microvalve array for addressable multiplex syntheses and assays. *J Micromech Microeng* 16:1433–1443.
18. Bretherton FP (1961) The motion of long bubbles in tubes. *J Fluid Mech* 10:166–188.
19. Baldessari F, Homsy GM, Leal LG (2007) Linear stability of a draining film squeezed between two approaching droplets. *J Colloid Interface Sci* 307:188–202.
20. Niu X, Gulati S, Edel JB, deMello AJ (2008) Pillar-induced droplet merging in microfluidic circuits. *Lab Chip* 8:1837–1841.
21. Utada AS, Fernandez-Nieves A, Stone HA, Weitz DA (2007) Dripping to jetting transitions in coflowing liquid streams. *Phys Rev Lett* 99:094502.
22. Zeng Y, Novak R, Shuga J, Smith MT, Mathies RA (2010) High-performance single cell genetic analysis using microfluidic emulsion generator arrays. *Anal Chem* 82:3183–3190.
23. Lee C, Lee S, Shin S, Hwang S (2007) Real-time PCR determination of rRNA gene copy number: absolute and relative quantification assays with *Escherichia coli*. *Appl Microbiol Biotechnol* 78:371–376.
24. Navin N, et al. (2011) Tumour evolution inferred by single-cell sequencing. *Nature* 472:90–94.
25. Stark M, Berger S, Stamatakis A, von Mering C (2010) MLTreeMap—accurate Maximum Likelihood placement of environmental DNA sequences into taxonomic and functional reference phylogenies. *BMC Genomics* 11:461.
26. Powell S, et al. (2011) eggNOG v3.0: Orthologous groups covering 1133 organisms at 41 different taxonomic ranges. *Nucleic Acids Res* 40:D284–D289.
27. Huson DH, Mitra S, Ruscheweyh H-J, Weber N, Schuster SC (2011) Integrative analysis of environmental sequences using MEGAN4. *Genome Res* 21:1552–1560.
28. Pernthaler A, et al., ed. (2008) Diverse syntrophic partnerships from deep-sea methane vents revealed by direct cell capture and metagenomics. *Proc Natl Acad Sci USA* pp:7052–7057.
29. Orphan VJ (2009) Methods for unveiling cryptic microbial partnerships in nature. *Curr Opin Microbiol* 12:231–237.
30. Lens P, O'Flaherty V, Moran AP, Stoodley P, Mahony T, eds. (2003) *Biofilms in Medicine, Industry and Environmental Biotechnology: Characteristics, Analysis and Control* (IWA, London).
31. Kolenbrander PE (1988) Intergeneric coaggregation among human oral bacteria and ecology of dental plaque. *Annu Rev Microbiol* 42:627–656.
32. Kolenbrander PE (1989) Surface recognition among oral bacteria: Multigeneric coaggregations and their mediators. *Crit Rev Microbiol* 17:137–159.
33. Lancy P, Jr, Appelbaum B, Holt SC, Rosan B (1980) Quantitative in vitro assay for "corncob" formation. *Infect Immun* 29:663–670.
34. Valm AM, et al. (2011) Systems-level analysis of microbial community organization through combinatorial labeling and spectral imaging. *Proc Natl Acad Sci USA* 108:4152–4157.
35. Shim J-u, et al. (2007) Control and measurement of the phase behavior of aqueous solutions using microfluidics. *J Am Chem Soc* 129:8825–8835.
36. Schmitz CHJ, Rowat AC, Koster S, Weitz DA (2009) Dropspots: A picoliter array in a microfluidic device. *Lab Chip* 9:44–49.
37. Huebner A, et al. (2009) Static microdroplet arrays: A microfluidic device for droplet trapping, incubation and release for enzymatic and cell-based assays. *Lab Chip* 9:692–698.